Cement 23 (2026) 100168

Contents lists available at ScienceDirect

Cement

journal homepage: www.sciencedirect.com/journal/cement

Production and properties of amorphous silica extracted from olivine for use as a supplementary cementitious material

Pei B. Ong, Yixiu Zhuge, Christopher Cheeseman, Hong S. Wong *

Department of Civil and Environmental Engineering, Centre for Infrastructure Materials, Imperial College London, London SW7 2BU, United Kingdom

ARTICLE INFO

Keywords:
Amorphous silica
SCM
Thermal treatment
Olivine
Low-carbon cements

ABSTRACT

Amorphous precipitated silica (APS) produced by acid leaching of olivine has been characterised and assessed for use as a supplementary cementitious material (SCM). The APS was thermally treated between 400 and 1000°C to modify its pore structure, surface area, composition and reactivity. Pastes and mortars containing APS were cast with CEM I replacement levels from 0 to 30 wt.% and water-to-binder ratio of 0.5. TGA-MS, Q-XRD, FTIR and R^3 tests show that APS has moderate to high pozzolanic reactivity. Mortars with 10 wt.% as-produced APS showed 30% increase in 28-day compressive strength compared to the control (50 MPa). Mortars with 20 wt.% replacement had comparable strengths to the control. Thermal treatment moderately reduced APS specific surface area and water demand, and improved mix workability, with mortars retaining comparable strengths to samples containing as-produced APS. The research demonstrates that silica derived from olivine has potential to be used as an SCM.

1. Introduction

Portland cement (PC) production contributes ~8% of global anthropogenic carbon emissions. These originate primarily from the carbon-based fuel combustion, decomposition of calcium carbonate during thermal treatment, and energy used in grinding clinker [1–5]. An effective climate mitigation strategy is to partially replace PC with low-carbon supplementary cementitious materials (SCMs). By-products from industrial processes such as ground granulated blast-furnace slag (GGBFS) and coal fly ash (FA) have been extensively used as SCMs [6,7]. The availability of GGBFS and FA is declining in some regions due to the closure of coal-fired power plants and the transition to electric arc furnaces for steel production [8,9]. This, combined with increasing global demand for PC, highlights the need for alternative sources of SCMs [1,2,10].

Magnesium silicate minerals are abundant, with estimated deposits of 1.4×10^5 billion tonnes [11]. Magnesium silicates such as olivine $(Fe, Mg)_2SiO_4$, can produce pozzolanic amorphous precipitated silica (APS) [11–13]. The extraction process typically uses sulphuric acid (H_2SO_4) or hydrochloric acid (HCl) and produces APS, magnesium salts and water as the main products as shown in Eqs. (1) and (2) [11–19]:

$$Mg_2SiO_{4(s)} + 2H_2SO_{4(aq)} \rightarrow 2MgSO_{4(aq)} + SiO_{2(s)} + 2H_2O_{(l)} \quad (1)$$

$$Mg_2SiO_{4(S)} + 4HCl_{(aq)} \rightarrow 2MgCl_{2(aq)} + SiO_{2(s)} + 2H_2O_{(l)} \quad (2)$$

The high-viscosity suspension containing APS can be separated from the magnesium-rich solution using centrifugation, vacuum filtration or salt-induced liquid phase separation [11–13,15,17,18]. Electrolysis produces magnesium hydroxide ($Mg(OH)_2$), which reacts with CO_2 to form magnesium carbonate [11]. Alternatively, ammonium hydroxide (NH_4OH) and CO_2 gas can be used to produce the hydrated magnesium carbonate nesquehonite ($MgCO_3{\cdot}3H_2O$) [20]. 1.3 tonnes of $Mg(OH)_2$ can sequester 1 tonne of CO_2 under controlled conditions [11]. Based on theoretical CO_2 uptake from magnesium sulphate carbonation, acid leaching of olivine has been proposed as a route to producing a lower-carbon pozzolanic silica. These estimates are based on stoichiometric calculations, and no life cycle assessment or carbon accounting study has been reported to date.

Amorphous precipitated silica (APS) has previously been extracted from olivine [11–15,17–21]. The APS physical and chemical properties are highly dependent on the production process and particularly reaction temperature, olivine particle size and solution pH [13,14,17,22]. The specific surface area (SSA) of APS, determined using N_2 adsorption and desorption, typically varies from 100 to 700 m^2/g [12,15,18]. Higher reaction temperatures (>50°C) and the use of larger olivine particles forms APS with lower SSA. The pH of the solution has a critical

* Corresponding author.
E-mail address: hong.wong@imperial.ac.uk (H.S. Wong).

https://doi.org/10.1016/j.cement.2025.100168

Available online 2 January 2026

role in determining particle stability. At low pH (0.5 to 1.0), colloidal APS becomes unstable and agglomerates, driven by the catalytic action of H^+ ions [15]. Longer reaction times allow more agglomeration, resulting in larger particles with increased porosity [15,18].

High SSA can significantly impact the performance of APS as an SCM [13,14,17,22]. This increases water demand and adversely affects workability. In previous research, this limited APS replacement levels of PC to a maximum of 2 wt.% [18]. Replacement levels up to 30 wt.% have been used, but this previous work focused on the hydration behaviour, pozzolanic reactivity and mechanical performance [12]. The impact of the SSA of APS on cement paste and mortar workability was not reported.

Thermal treatment has been used to reduce the SSA of aluminosilicates, Stöber silica, amorphous nano-silica and commercial silica gels [23–26]. Heating to temperatures between 500 and 800°C collapses micropores and condenses hydroxyl groups into siloxanes, resulting in a significant reduction in SSA [24,25,27]. At higher temperatures (>800°C), further densification and structural changes occur, with amorphous silica crystallising to form cristobalite [23,24]. Alkaline solutions have also been used to accelerate silica dissolution and reduce the SSA [24,28].

While previous work indicates the feasibility of using thermal treatment to modify silica, the potential changes in reactivity, morphology, and phase composition have not been reported. The aim of this work was therefore to evaluate APS derived from olivine as a supplementary cementitious material (SCM) through a systematic series of characterisation and performance tests. Key properties of APS, including chemical composition, crystalline phases, specific surface area, and the impact of APS on mortar workability and mechanical performance are assessed. The potential of using thermal treatment to improve the properties of APS as an SCM is also reported.

2. Materials and methods

2.1. Materials

Olivine ($(Fe,Mg)_2SiO_4$, supplied by Sibelco), Portland cement (CEM-I 52.5N, Breedon Group plc, compliant with BS EN 197-1), and microsilica (Elkem Microsilica Grade 983-U) were used. Their chemical composition and physical properties are shown in Table 1 and Table 2 respectively. Siliceous sand with particle size < 4 mm and a water absorption of 0.77 wt.% (ASTM C128–22) was used in mortar samples. This was oven-dried at 105°C prior to use. A superplasticiser (Visco Flow 3000, from SIKA) was used to control mix workability.

2.2. Preparation of APS

100 g of olivine was added to 500 mL of 3M H_2SO_4 solution on a hot plate set at 80 ± 5°C, and the mix continuously stirred for 90 minutes. To facilitate smooth transfer and separation, an additional 100 mL of deionised water was added to the suspension. The mixture was then centrifuged (Eppendorf 5910Ri) at 4000 rpm for 90 s in 250mL tubes. This caused the APS and inert solids to form at the bottom of the tubes, while the Mg-rich supernatant formed on the top. The APS was collected, and dried at 105°C, ground with a mortar and pestle and washed with deionised water using a Buchner funnel and vacuum flask to remove residual Mg and Fe cations and sulphate anions. The washed APS was dried at 105°C for 24 hours and passed through a 300-μm mesh to form the homogenous powder used in subsequent experiments.

Table 2
Physical properties of olivine, CEM-I, microsilica and APS.

	Density (kg/m^3)	Specific surface area (m^2/g)	Particle size distribution (μm)		
			D_{90}	D_{50}	D_{10}
Olivine	3110	4.45	54.3	16.1	3.32
CEM-I	3106	1.22	50.2	16.9	3.10
Microsilica	2280	16.4	33.1	9.82	0.445
APS	2240	249	205	63.1	11.6

2.3. Thermal treatment of APS

50 g samples of APS were thermally treated in 50 ml Al_2O_3 crucibles by heating at 400, 500, 750, 800, 850, 900, 950 and 1000°C for 60 minutes (Lenton SAF 11/1 furnace). The selected temperatures represent main decomposition and phase transformation events deduced from thermogravimetric analysis of APS (Section 3.2). After heating, the samples were air cooled naturally to room temperature (~23°C). Trials were carried out with water quenching to see if this increased reactivity, but results showed no significant difference. Thermally treated APS was then tested to evaluate their performance as SCM. As-produced amorphous precipitated silica is denoted as APS, while thermally treated APS are referred to as XXXA, where XXX indicates the treatment temperature in°C (e.g., 400A, 900A).

2.4. Mix designs

Cement pastes with 0, 10, 20, and 30 wt.% APS replacement levels at water-to-binder (w/b) ratio of 0.5 were mixed and cast into 20 mm cubes. Samples were vibrated until no air bubbles escaped from the surface. After casting, the samples were covered with a damp cloth and sealed with an impermeable plastic membrane for 24 hours, before being demoulded and cured at 20 ± 2°C and 95 ± 5% RH. Samples were crushed using an agate mortar and pestle after curing for 7 and 28 days and hydration stoppage by solvent exchange using isopropanol [29]. The powdered samples were stored in low vacuum (0.2 bar) with silica gel and soda lime to minimise carbonation, prior to analysis using TGA, XRD, and FTIR (Table 3).

Mortar samples were prepared at cement replacement levels of 0, 10, 20, and 30 wt.% APS. The samples had a sand-to-binder ratio of 3:1 and a w/b ratio of 0.5. Mix designs are shown in Table. Mixes were designated as ACMXX for mortars with as-produced APS or TACMXX for those containing thermally treated APS at 900°C, where XX denotes the replacement level (e.g., ACM10 = 10 wt.% as-produced APS; TACM20 = 20 wt.% thermally treated APS at 900°C). PCM is the plain cement mortar control sample. The superplasticiser dosage used in these mixes follows the range reported in earlier studies on APS systems, where 1–2 wt.% has been shown to be necessary to obtain workable pastes [12,30].

Mortar components were mixed for 30 s, using a NG-AutoDigiMix 2 mortar mixer, prior to the addition of water. Wet mixing was carried out for 90 s at low speed, followed by 30 s of manual mixing and 90 s at high

Table 1
XRF analysis on olivine, CEM-I, microsilica and APS.

	Composition (%)									
	SiO_2	MgO	Fe_2O_3	Al_2O_3	K_2O	CaO	SO_3	Others	LOI	Total
Olivine	40.7	47.0	7.00	0.90	0.10	0.10	-	1.00	3.20	100.0
CEM-I	20.9	0.39	2.68	6.62	0.78	60.1	6.02	0.70	1.70	99.9
Microsilica	98.7	0.09	0.04	0.38	0.26	0.20	0.08	0.18	0.1	100.0
APS	77.0	6.30	0.90	0.60	-	-	2.30	1.20	11.8	100.1

Table 3
Mix design of PC and APS paste and mortar.

Sample ID	Cement (g)	APS (g)	900A (g)	Water (g)	Sand (g)	Superplasticiser (g)
PC	1000	0	0	500	0	0
AC10	900	100	0	500	0	0
AC20	800	200	0	500	0	0
AC30	700	300	0	500	0	0
PCM	1000	0	0	500	3000	0
ACM10	900	100	0	500	3000	20
ACM20	800	200	0	500	3000	20
ACM30	700	300	0	500	3000	20
TACM10	900	0	100	500	3000	20
TACM20	800	0	200	500	3000	20
TACM30	700	0	300	500	3000	20

speed. The mortar mixes were tested for water demand and workability, and then cast into 50 mm cubes and compacted on a vibration table for 2 minutes. Mixes with 30 wt.% APS were particularly dry and required manual compaction with a tamper. After casting, the mortar cubes were covered with a damp cloth and plastic membrane for 24 hours and cured in water at 20 ± 2°C for 1, 3, 7, 28 and 90 days.

2.5. Characterisation tests

Chemical analysis used X-ray fluorescence (Malvern Panalytical Zetium XRF), with samples prepared as glass disks formed at 1050 °C (LeNeo Fusion furnace) using lithium borate fusion. 0.9 g of APS was placed in a platinum crucible with 9 g of lithium borate. The contents were thoroughly mixed to ensure homogeneity. Ten drops of lithium iodide were added to enhance the fusion process. The platinum crucible containing the mix was placed in a preheated furnace. The melted material was cooled to form solid glass disks that were analysed using the Zetium XRF system, with data processed using SuperQ Spectra software.

Thermogravimetric analysis (TGA) was used to characterise the changes in physical and chemical properties of APS and cement paste samples. The analysis was performed using NETZSCH STA449 F5 coupled with QMS 403 Aëolos Quadro mass spectrometer (MS) to detect gases released during heating. 50 ± 0.1 mg of sample in an alumina crucible was heated to a maximum temperature of 1050°C at a heating rate of 10 K/min with N_2 gas flowing at 50 mL/min to maintain an inert atmosphere. Differential thermogravimetric (DTG) analysis was used to identify temperature ranges with significant mass loss.

TGA of cement paste samples allowed the determination of bound water from the mass loss between 40°C to 600°C, portlandite content from the mass loss between 420°C and 520°C, and calcium carbonate (CC) content from the mass loss between 600°C to 850°C. Portlandite content $CH_{measured}$ was calculated using the molar masses of calcium hydroxide ($M_{Ca(OH)_2} = 74g/mol$) and water ($M_{H_2O} = 18g/mol$), and was normalised to the mass of PC in each mix to allow comparisons. Calcium carbonate content was also quantified using the same method.

In cement pastes containing APS, the theoretical portlandite content ($CH_{theoretical}$) assuming no pozzolanic reaction was calculated to account for the reduction in PC content caused by APS replacement. A reference portlandite content for pure PC cement paste was first determined from TGA. The theoretical portlandite content in APS-blended systems was then calculated by scaling the reference portlandite content according to the PC fraction in the mixture. Comparing the portlandite content ($CH_{measured}$) in APS-containing mixes to the theoretical portlandite content allowed estimation of portlandite consumption due to pozzolanic reactions.

Quantitative X-ray diffraction (Q-XRD, Malvern Panalytical Empyrean XRD) was used to characterise the crystalline phases in olivine, APS, thermally-treated APS, anhydrous PC, and hydrated cement pastes. XRD used Cu Kα radiation generated with a Cu X-ray tube operated at 45 kV and 40 mA. Diffraction data were recorded from 5° to 90° 2θ, with a step size of 0.02° per second. Internal standard quantification was used by mixing 0.8 g of powdered sample with 0.2 g corundum (Al_2O_3), and this was ground with a mortar and pestle for 20 minutes to ensure homogeneity. Data was analysed using HighScore Plus software with the ICDD database, with each sample tested three times to obtain average data.

The degree of hydration of cement pastes was determined using Q-XRD. The phase composition of anhydrous Portland cement (C_3S, C_2S, C_3A, C_4AF, and gypsum) was first quantified using Q-XRD. For APS-containing mixes (AC10, AC20 and AC30), the initial cement phase composition was calculated by scaling the measured composition of anhydrous PC according to the cement fraction in each mix. Comparison between the unreacted and hydrated phase composition enabled calculation of the degree of hydration as a fraction of reacted cement phases over the initial content, expressed as a percentage.

Fourier-transform infrared spectroscopy (FTIR, Thermo Scientific Nicolet iS40 spectrometer) was used to investigate the surface functionalities of as-produced APS, thermally-treated APS, and microsilica. Each sample was tested three times, using 64 scans per test at a resolution of 4 cm^{-1} over a wavenumber range from 400 to 3900 cm^{-1}.

The specific surface area (SSA), total pore volume (1.7 nm to 300 nm), and average pore diameter of APS samples were analysed using gas adsorption (Micromeritics 3Flex 3500) to evaluate the effects of thermal treatment. Samples (0.2000g ±0.0001g) were degassed at 40°C for 24 h, then cooled to room temperature and tested with N_2 gas. The SSA was calculated using the Brunauer-Emmett-Teller (BET) method. Pore size and total pore volume were calculated using the Barrett-Joyner-Halenda (BJH) method.

The reactivity of APS, thermally treated APS, and microsilica were evaluated using the R^3 test (ASTM C1897–20) [31]. This determines pozzolanic reactivity from isothermal conduction calorimetry (ICC). The test pozzolan was mixed with calcium hydroxide (~ 98% purity, Thermo Scientific) and calcium carbonate (≥ 99% purity, Sigma-Aldrich) at a mass ratio of 1:3:0.5. A potassium solution was prepared by dissolving 4 g of potassium hydroxide (~ 88.2% purity, VWR chemicals) and 20 g potassium sulphate (≥ 99% purity, Sigma-Aldrich) in 1 L of deionised water. The test sample, potassium solution and ICC were equilibrated at 40°C for at least 24 hours prior to use. The test sample was combined with the potassium solution at a 1:1.2 ratio. 15 g of the resulting paste was transferred into the calorimeter and monitored for 7 days, with 9.4 g deionised water as a reference. The cumulative heat released was determined per mass of SCM (J/g) in the paste sample. Three replicates were tested and the results averaged.

Water demand was determined using a flow table on mortars containing APS. The test identifies the w/b ratio required for mortars with varying APS replacements to achieve the same flow as the PC-only control mortar at 0.5 w/b ratio. The sand-to-binder ratio was at 3:1. The starting w/b ratio was 0.5, and this was increased by increments of 0.05 until the target flow spread of 115 mm was achieved. The flow table test was conducted in accordance with BS EN 12350-5:2019 [32], and each measurement was repeated three times to obtain an average spread diameter.

The flow table was also used to evaluate the effect of APS and superplasticiser on mortar workability. This was performed at constant w/b ratio of 0.5, with superplasticiser added at 0, 1 and 2 wt.% of the binder content (BS EN 12350-5:2019). Mortars with 100% PC (control samples) and APS replacement levels of 10, 20 and 30 wt.% were tested. Flow table measurements were conducted three times for each sample using freshly mixed mortar, with all measurements taken exactly seven minutes after initial mixing to ensure consistency.

Compressive strength tests were conducted at 1, 3, 7, 28, and 90 days on mortar containing APS and thermally treated APS at 0.5 w/b ratio. The tests on 50 mm cube samples used an automatic compression machine (Controls Automax 5) at a loading rate of 0.3 MPa/s. Three cubes were tested per mix and curing age, and the average compressive strength calculated.

The connected porosity of mortar samples was determined by water absorption in accordance with ASTM C642 on samples with a w/b ratio of 0.5 hydrated for 7 days [33]. The apparent porosity was calculated using Archimedes principle [34]. Water absorption and apparent porosity were calculated from the mass of 50 mm cubes in water-saturated condition, oven-dried at 105°C, and suspended in water. Three replicate cubes were tested and the results averaged.

3. Results

3.1. Material characterisation data

The chemical composition of olivine, CEM-I, microsilica and APS, determined by X-ray fluorescence (XRF), are shown in Table 1. Basic physical property data, including density and particle size distributions (D_{10}, D_{50}, D_{90}), are given in Table 2.

The production of APS from olivine was confirmed by XRD, as shown in Fig. 1a. Forsterite, biotite, and lizardite are present in the raw olivine, but absent in the APS. This shows effectiveness of the dissolution. Clinochlore, chabazite, enstatite, and cordierite are acid-resistant and remained in minor quantities. The broad 'amorphous hump' in the XRD data between 15° and 30° (2θ) indicates formation of an amorphous silica network. XRD peaks associated with magnesium and iron sulphates, which typically appear between 25° and 30° (2θ) were not detected in APS, indicating that the centrifugation and washing steps effectively removed residual sulphates.

Fig. 1(b) shows the macroscopic appearance of the raw olivine and extracted APS. The olivine appears green-to-grey, while APS is noticeably whiter, reflecting the loss of Fe-bearing dissolved components. This aligns with the mineralogical changes detected by XRD and supports the conclusion that acid leaching effectively produces amorphous silica. This is confirmed by XRF chemical analysis (Table 1) that shows APS contained 77.0% SiO_2 with significantly reduced Mg and Fe content compared to the raw olivine. Dissolution of Mg and Fe bearing phases during acid leaching, forms soluble sulphate salts that were subsequently removed by centrifugation and washing. The residual Mg content in APS is due to acid-resistant Mg-bearing minerals such as enstatite.

Fig. 1(c) shows the FTIR spectrum of the raw olivine. In addition to a small O–H feature near 3680 cm^{-1}, the olivine sample exhibited Mg/Fe–O vibrational peak at 607 cm^{-1} and a shoulder at 493 cm^{-1}, which may also include contributions from Si–O lattice modes, reflecting high Mg and Fe content. A broad double-peak Si–O region is also visible between 1150–715 cm^{-1}, consistent with the presence of silicate minerals. Fig. 1(d) compares the FTIR spectra of APS with microsilica. Both materials exhibited major silica vibrations but differ in certain hydroxyl

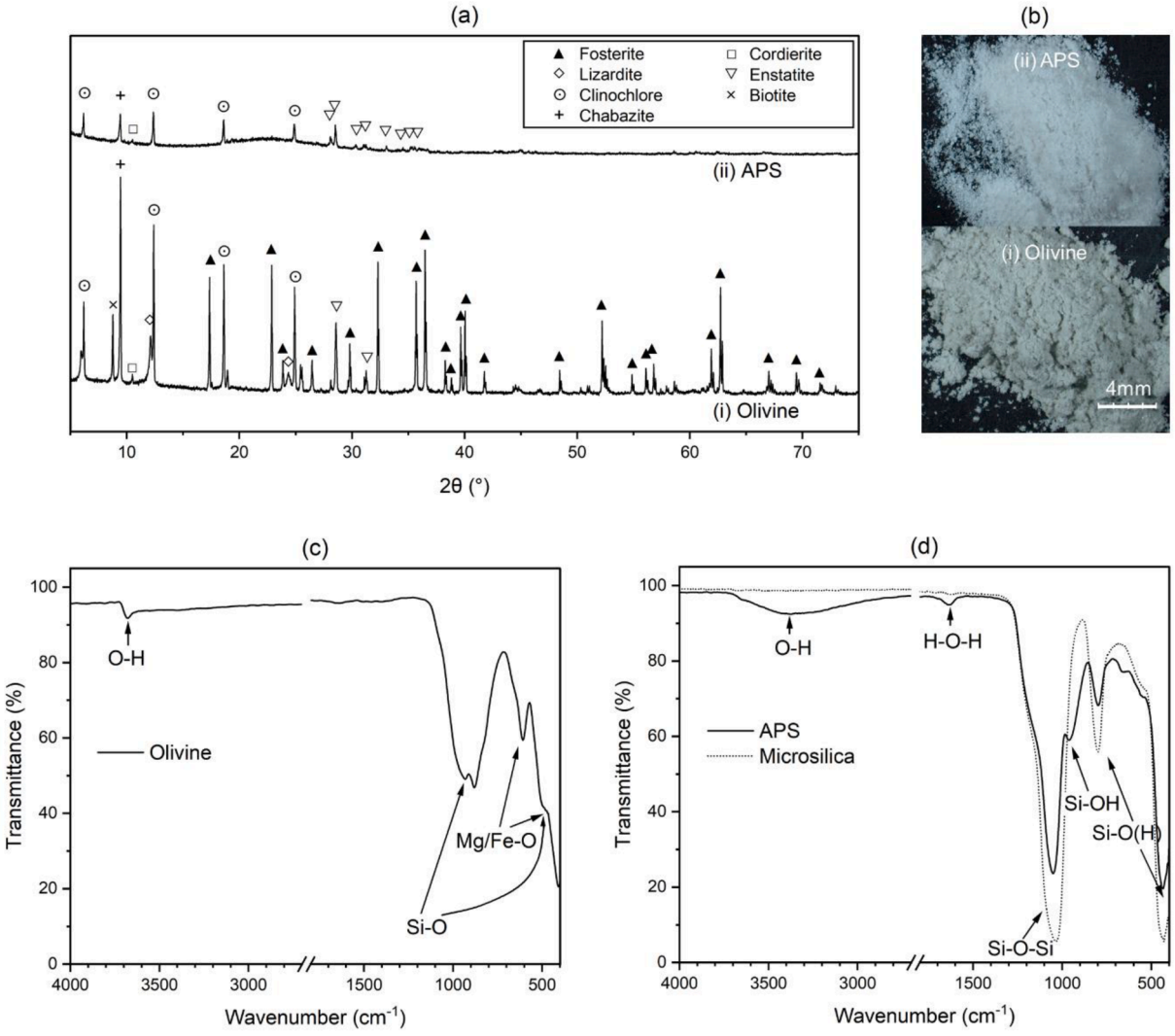

Fig. 1. (a) X-ray diffraction data of olivine and APS; (b) colour transition from olivine to APS; (c) FTIR spectra of olivine and (d) APS, with microsilica included as a reference.

features. A broad band near 3400 cm^{-1} represents O–H stretching vibrations from silanol groups and adsorbed water, indicating higher surface hydroxylation and moisture content in APS [27,35–38]. The region around 1600–1700 cm^{-1} corresponds to H–O–H bending vibrations of molecular water, further confirming the presence of physically bound moisture in APS [27,36–38].

A strong absorption near 1080 cm^{-1} signifies the asymmetric stretching of Si–O–Si bonds and reflects the integrity of the silica framework [27,36–38]. Interestingly, APS has a shoulder peak at approximately 950 cm^{-1}, which is indicative of Si–OH stretching. This suggests high levels of surface hydroxylation and possible defects within the APS silica network. The band near 800 cm^{-1} signifies symmetric Si–O(H) stretching modes, while the absorption around 460 cm^{-1} corresponds to Si–O(H) bending vibrations, both representing fundamental silica structural units [27,36,39–41]. The larger OH-related signals in APS, combined with relatively weaker Si–O–Si peaks, indicate a more disordered and hydroxyl-rich structure compared with the reference microsilica [42,43].

3.2. Effect of thermal treatment

TGA-MS was conducted on APS to study structural changes during thermal treatment. The results, presented in Fig. 2(a), show several distinct stages of mass loss. The first stage between 80°C and 200°C (6.1% mass loss), is attributed to evaporation of surface-adsorbed water. This is confirmed by mass spectroscopy which identified water vapour (m/z = 18) as the primary gas released. Between 200°C and 500°C, mass loss was minimal, indicating that the APS structure is stable in this temperature range. The final stage, between 500°C and 1050°C, exhibited a gradual mass loss of 5.26% due to condensation of silanol groups within APS and dehydroxylation of impurities such as Mg-bearing solids [17], indicating alteration of the crystalline structure of these residual phases.

The colour changes in APS on heat treatment are shown in Fig. 2b. Minimal discolouration occurs up to 500°C, but oxidation of trace Fe ions causes a beige hue at higher temperatures, as shown in Fig. 2b-*iii* and *b-iv*. This observation is consistent with XRF results (Table 1), which showed that APS has reduced Fe content.

The XRD patterns for APS and thermally treated APS (Fig. 2c-*i* to *a-ix*) show that the diffuse scattering between 15° and 30° (2θ) intensified with increasing temperature, which indicates enhanced structural disorder in the silica network. Peaks at 5°–25° (2θ), associated with residual crystalline phases clinochlore, chabazite and cordierite, diminished at 750°C and disappeared entirely by 950°C. Fig. 2(d) compares the crystalline and amorphous fractions of APS, heat-treated APS and microsilica from Q-XRD. Thermal treatment below 500°C had no significant effect on the crystalline phases in APS, with the untreated APS, 400A, and 500A showing approximately 80 wt.% amorphous

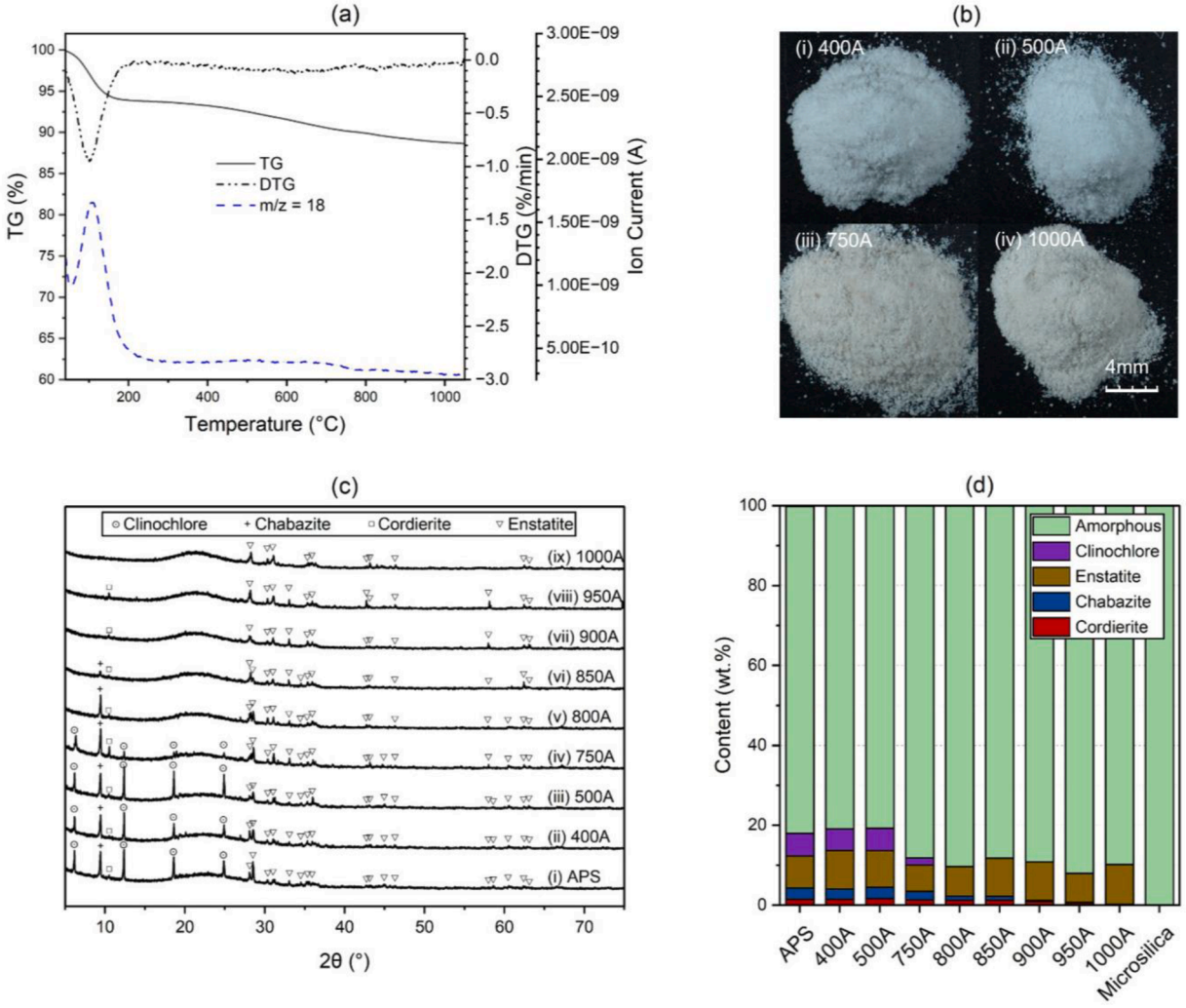

Fig. 2. (a) TGA-MS data of APS derived from olivine; (b) colour transition of thermally treated APS. (c) XRD pattern of as-produced APS and thermally treated APS at 400°C – 1000 °C (i – ix); (d) Q-XRD of crystalline and amorphous phases present in APS, heat-treated APS and microsilica. 400A–1000A denote APS thermally treated at the corresponding temperatures in°C.

content and 20 wt.% inert solids. By 750°C, the amorphous content increased to ~88 wt.%, coinciding with a decline in clinochlore content. This trend continued, with clinochlore becoming fully amorphous at 800°C, consistent with calcination temperatures reported in the literature [44,45]. Additionally, chabazite gradually decreased between 750 and 800°C, becoming amorphous at 900°C, as reported in other studies [46,47]. Cordierite disappeared by 950°C. Beyond this temperature, the amorphous content plateaued at approximately 90%–93%, with enstatite being the only crystalline phase remaining at 1000°C. The results show that most impurities in APS become amorphous at high temperatures, with the transformation of clinochlore, chabazite, and cordierite accounting for the observed increase in amorphous content. Variations in the crystalline phases suggest heterogeneity of the olivine feedstock composition.

Fig. 3 illustrates the FTIR spectra of thermally treated APS. Below 500°C, hydroxyl- and silica-related bands decrease slightly, suggesting that mild heating primarily removes loosely adsorbed water without significantly altering the silica network itself. Increasing the treatment temperature to 750°C significantly lowers the O–H stretching and bending signals (Fig. 3b,c), completely removing the Si–OH-related feature near 960 cm^{-1} (Fig. 3e). These observations indicate that higher temperatures promote the condensation of surface hydroxyl groups, reduce defect sites and thereby leading to a more compact silica structure with fewer hydrophilic species. Further heating to 800°C eliminates nearly all moisture- and hydroxyl-associated signals, leaving only the silica framework peaks around 800 cm^{-1} and 1050 cm^{-1}. This near-complete elimination of hydroxylation and adsorbed water suggests a transition towards a more stable, predominantly siliceous network. Above 800°C, minimal changes were observed, apart from a slight reduction in Si–O–Si stretching intensity (Fig. 3d), possibly reflecting progressive disruption of the silica network and formation of simpler Si–O bonds.

Fig. 4 shows the effect of thermal treatment on the average specific surface area (SSA), pore diameter, and total pore volume of APS. The error bars show ± 1 standard error. The SSA of untreated APS is approximately 250 m^2/g, significantly higher than that of microsilica (16 m^2/g). Thermal treatment at 400°C and 500°C did not substantially alter the SSA or average pore diameter, indicating minimal changes in pore structure below 500°C. However, at 750°C, a significant reduction in SSA to ~180 m^2/g is observed, accompanied by an increase in pore diameter and a reduction in total pore volume, suggesting pore closure and structural compaction. With further increase in temperature, SSA and total pore volume steadily declined, reaching ~100 m^2/g and 0.36 cm^3/g at 1000°C. These results show that thermal treatment of APS at temperatures greater than 500°C cause significant structural evolution characterised by densification and pore closure.

3.3. Pozzolanic reactivity

The pozzolanic reactivity of APS and thermally treated APS was evaluated using the R^3 test, with microsilica included as a reference. Results are shown in Fig. 5; A benchmark of 330 J/g (at 7 days) was used to distinguish "highly reactive" from "moderately reactive" SCMs, in line with established classification method using the regression model for silica fume [48].

Microsilica exhibited high reactivity, releasing 378 J/g at 3 days and 477 J/g at 7 days. The as-produced APS achieved cumulative heat of 236 J/g at 3 days and 249 J/g at 7 days, which is classified as moderately reactive [48]. Thermally treated APS showed higher heat release, consistent with their increased amorphous content. The maximum reactivity was achieved at 900°C, where the cumulative heat reached 351 J/g at 3 days and 381 J/g at 7 days. APS treated at 1000°C exhibited lower reactivity; since no quartz or cristobalite were detected in XRD or Q-XRD (Fig. 2c,d), this reduction in reactivity is attributed to the 60% loss of SSA (from 249 m^2/g in untreated APS to 99 m^2/g in 1000A), which reduces the amount of reactive sites available for reaction. Overall, the results show that thermal treatment enhances the pozzolanic activity of APS, with maximum improvement of 53% observed at

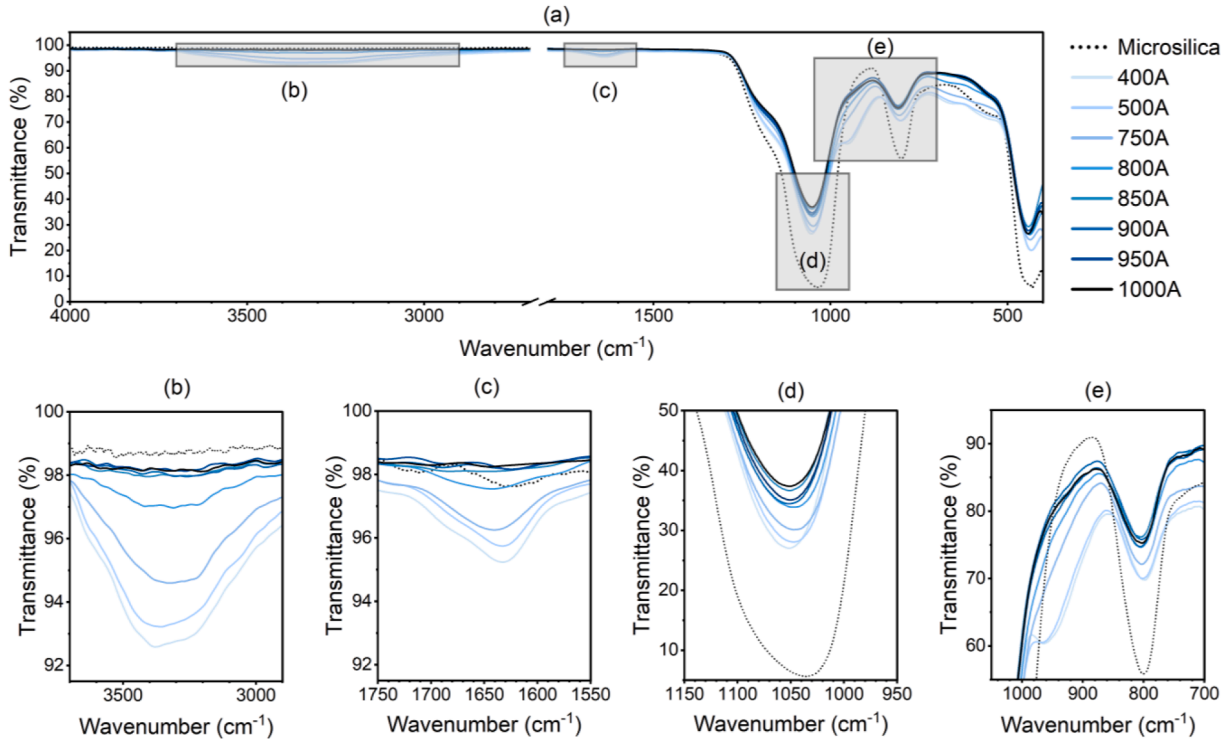

Fig. 3. FTIR spectra of thermally treated APS: (a) full spectrum ranging from 4000 cm^{-1} to 400 cm^{-1}; (b) enlarged region showing O–H stretching vibrations (2900–3700 cm^{-1}); (c) enlarged region highlighting H-O-H stretching vibrations (1600–1700 cm^{-1}); (d) Si–O–Si asymmetric stretching vibrations (1080 cm^{-1}); (e) combined Si–O(H) and Si–OH stretching vibrations (750–1000 cm^{-1}).

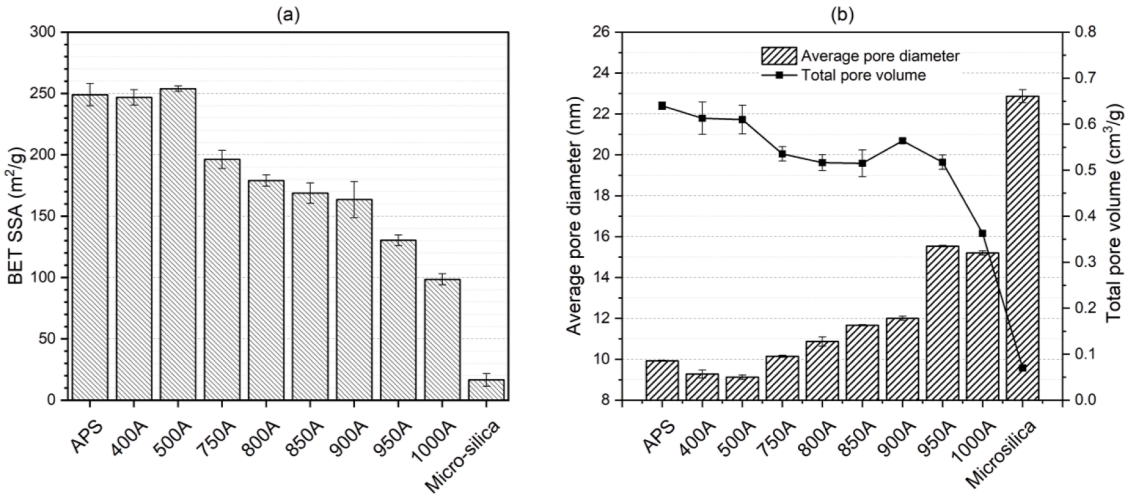

Fig. 4. Effect of thermal treatment on (a) BET specific surface area; and (b) BJH average pore diameter and total pore volume (1.7–300 nm) of APS. Microsilica is included as a reference.

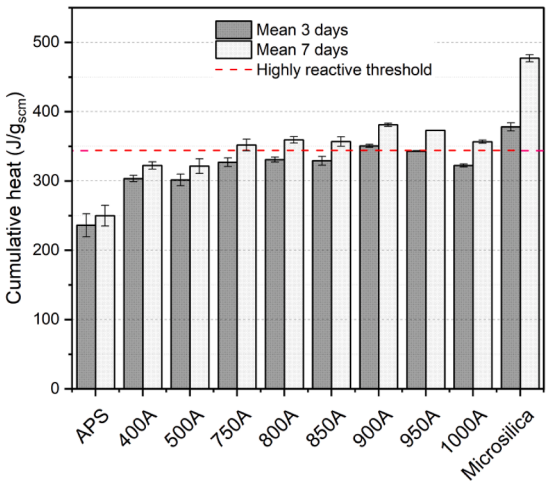

Fig. 5. Cumulative heat released as measured with the R^3 test method on APS, thermally treated APS and microsilica at 3 and 7 days. The threshold defining a "highly reactive" pozzolan was calculated using the regression model for silica fume stated in [47].

900°C. 900A was chosen to represent thermally treated APS to produce mortars in subsequent experiments.

TGA was used to further investigate the pozzolanic activity of as-produced APS in cement pastes containing 10 wt.%, 20 wt.% and 30 wt.% replacement. Fig. 6 shows mass loss and DTG curves at 7 and 28 days of hydration. Three major mass loss events were observed: dehydration of bound water from C-S-H and AFt phases (40–200°C), dehydroxylation of portlandite (420–520°C), and decomposition of calcium carbonate (600-850°C). The calculated contents of bound water, portlandite, and calcium carbonate are presented in Table 4. The results indicate a clear reduction in portlandite content with increasing APS replacement level. Portlandite content in most samples shows an increase at 28 days due to continuous hydration of PC and complete reaction of APS. However, in AC30, portlandite continued to decline, suggesting an excess of reactive silica relative to available CH.

The enlarged DTG regions at 80–160 °C (Fig. 6a* and 6*b**) show clear increases in the intensity of bound water loss with higher APS replacement level, and the loss is greater at 28 days. This suggests formation of additional hydration products such as C-S-H and AFt. Bound water quantification complemented these findings (Table 4). At 7 days, APS-containing pastes showed slightly lower bound water content compared to PC, which is consistent with the slower reaction kinetics of APS in early stages. At 28 days, all mixes showed increase in bound water content, confirming ongoing cement hydration and sustained pozzolanic activity of APS over time. However, no clear trend with increasing APS content was observed, likely due to the concurrent effects of cement hydration, pozzolanic reaction, and the intrinsic mass loss of APS during thermal analysis. This may introduce uncertainty in bound water estimation, particularly at higher replacement levels. Nevertheless, the use of tangential method and hydration stoppage provides consistency across samples and allows for comparative interpretation [43–46].

3.4. Phase assemblage

Fig. 7(a) presents the Q-XRD phase assemblage of the dry binder mixes before hydration. As the APS replacement level increased, the relative content of cement phases (C_3S, C_2S, C_3A, C_4AF, and gypsum) decreased, while the amorphous content increased due to the contribution of APS.

Fig. 7(b) and (c) show the phase assemblage of 7-day and 28-day hydrated pastes. At 7 days, PC contained 10 wt.% portlandite, whereas AC10, AC20, and AC30 showed lower contents at 5.4 wt.%, 1.7 wt.%, and 0.3 wt.%, respectively. At 28 days, portlandite increased in PC, AC10, and AC20 to 10.9 wt.%, 6.1 wt.%, and 2.0 wt.%, while AC30 remained low at 0.2 wt.%. These trends from Q-XRD correlate well with those observed from TGA (Table 4 and Fig. 6) although the absolute values differ. The trends reflect a balance between continued cement hydration with age (which increases portlandite formed) and pozzolanic reaction of the APS (which consumes portlandite). AC30 exhibited near complete portlandite depletion by 28 days and excess unreacted APS remained.

A general decrease in cement phases (C_3S, C_2S, C_3A, C_4AF, and gypsum) with curing age was observed across all mixes. The small and relatively negligible contribution of minor APS-derived phases (clinochlore, chabazite, cordierite, and enstatite, grouped as "Others" in Fig. 7) confirms that these minerals did not actively participate in hydration reactions. This supports the interpretation that the changes in phase assemblage are primarily governed by the dissolution of clinker minerals and subsequent formation of secondary reaction products.

Fig. 7(d) presents the degree of hydration, calculated based on the consumption of clinker phases. At 7 days, AC10 showed the highest degree of hydration (91.4%), slightly exceeding that of PC (88.9%), while AC20 and AC30 recorded 87.8% and 88.5%, respectively. The increase in AC10 may be attributed to filler or nucleation effects from

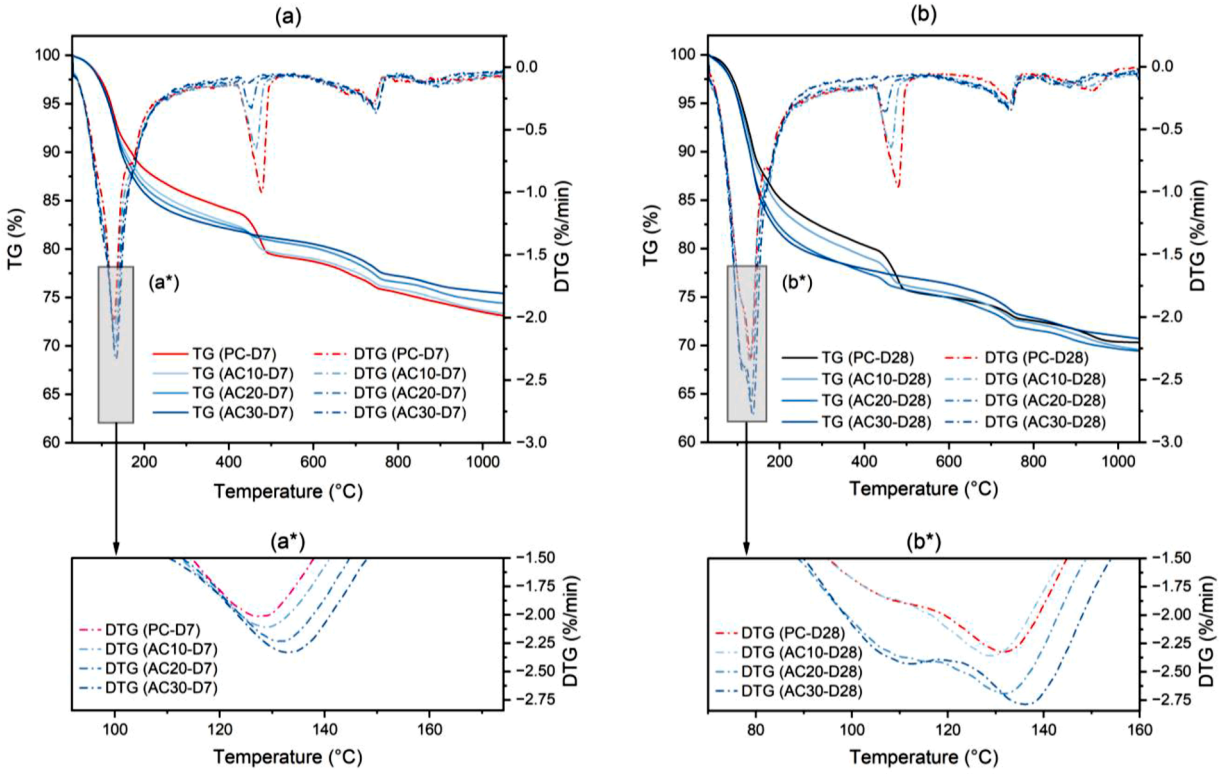

Fig. 6. (a) TGA of 7 days hydrated cement paste containing APS; (a*) Enlarged region showing dehydration of C-S-H and AFt phases; (b) TGA of 28-day hydrated cement paste containing APS; (b*) Enlarged region showing dehydration of C-S-H and AFt phases.

Table 4
Portlandite, calcium carbonate and bound water content (wt.%) in cement pastes.

Sample ID	Hydration age (days)	$CH_{theoretical}$ (wt.%)	$CH_{measured}$ (wt.%)	*CH* consumption (%)	*CC* (wt.%)	Bound water (wt.%)
PC-D7	7	16.5	16.5	-	3.03	21.3
AC10-D7		14.8	9.75	34	3.39	21.0
AC20-D7		13.2	3.74	72	4.75	19.9
AC30-D7		11.5	1.12	90	4.92	19.5
PC-D28	28	17.4	17.4	-	2.82	25.0
AC10-D28		15.7	10.1	36	3.52	24.6
AC20-D28		13.9	4.46	68	4.06	25.1
AC30-D28		12.2	0.56	95	4.72	23.7

APS, which enhances early hydration of cement. By 28 days, hydration degrees increased in all mixes. AC20 reached the highest value (94.2%), followed closely by AC10 (93.9%) and PC (93.2%). AC30 remained slightly lower at 91.9%, likely due to dilution of cement content and the associated reduction in available clinker for hydration.

Overall, Q-XRD results correspond to the TGA findings, as the observed trends in portlandite and amorphous content align with the bound water evolution, confirming that APS underwent pozzolanic reactions and contributes to hydration product formation. The effect was most evident at moderate replacement levels ($\leq$ 20 wt.%), where sufficient CH is available to sustain the reaction [27,34–38,41,42,47].

3.5. Water demand and workability

Fig. 8(a) shows the effect of as-produced and thermally treated APS on water demand of mortars. The reference mortar (PCM) achieved a flow spread diameter of 115 mm at 0.5 w/b ratio. Inclusion of APS increases water demand and w/b ratio to maintain comparable flow to the reference. At 10 wt.% replacement, ACM10 required a w/b ratio of ~0.61. For ACM20 and ACM30, the required w/b ratio increased to ~0.74 and ~0.85, respectively, representing a ~70% increase in water demand compared to PCM. This suggests a nonlinear relationship between APS content and water demand, where higher replacement levels lead to disproportionately greater losses in flowability.

Thermal treatment of APS at 900°C reduced water demand across all replacement levels, especially at 10% and 20%. TACM10 showed a similar w/b ratio to ACM10, while TACM20 and TACM30 required slightly less water than their untreated counterparts (~0.71 and ~0.81, respectively). These reductions are attributed to the decreased surface area and pore volume following thermal densification (see Section 3.2). However, the benefit of thermal treatment diminished at 30% replacement, where the absolute volume of porous APS probably outweighs the gains from structural densification. This suggests that the effectiveness of thermal treatment is limited at high APS contents.

The influence of superplasticiser (SP) on the workability of APS-containing mortars at 0.5 w/b ratio is depicted in Fig. 8(b). In mixes with 10 wt.% APS, both ACM10 and TACM10 responded well to SP addition, reaching or exceeding the reference flow with 1–2 wt.% SP. In contrast, the workability of ACM20, ACM30, and their thermally treated counterparts improved only marginally, even at the highest SP dosage (2 wt.%). Although thermal treatment of APS decreased SSA and reduced water demand, the improvement was insufficient to overcome the loss in

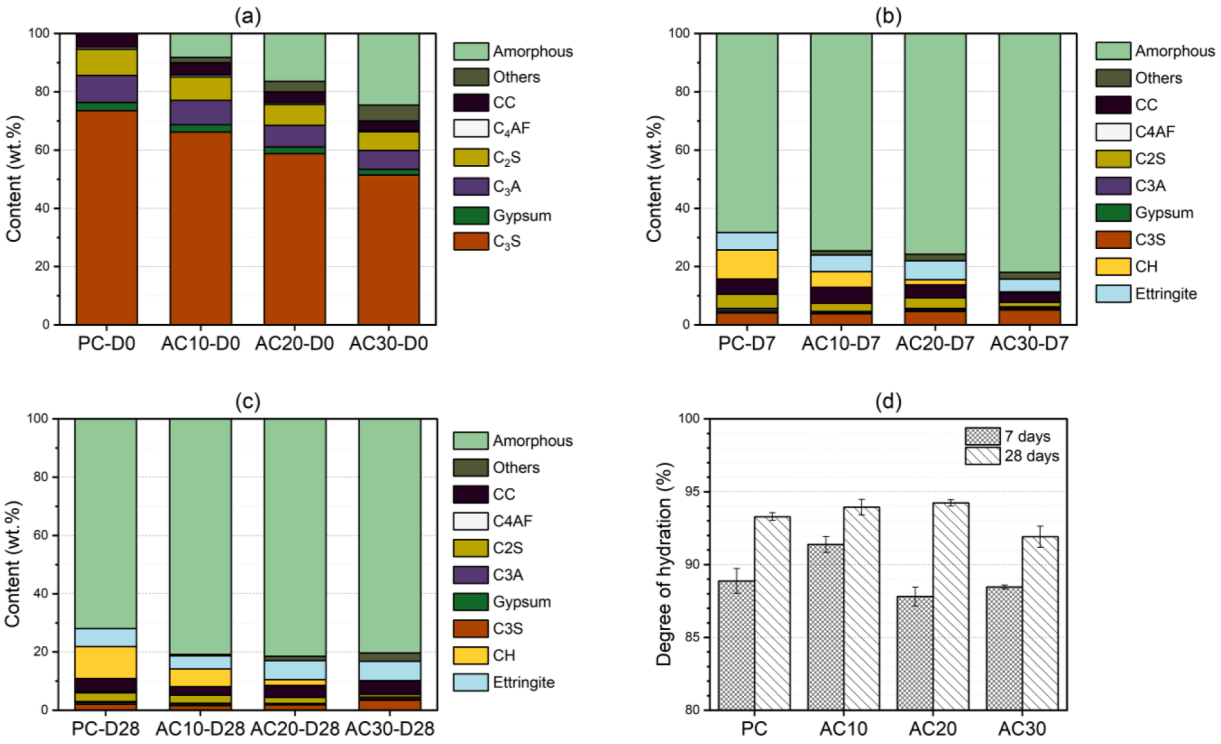

Fig. 7. Q-XRD phase assemblage of (a) dry binder mixes before hydration; (b) 7-day hydrated cement paste; and (c) 28-day hydrated cement paste; (d) Degree of hydration of cement pastes at 7 and 28 days. CH = portlandite; C_3S = tricalcium silicate; C_2S = dicalcium silicate; C_3A = tricalcium aluminate; C_4AF = tetracalcium aluminoferrite; CC = calcium carbonate; Others = clinochlore, enstatite, chabazite and cordierite from APS.

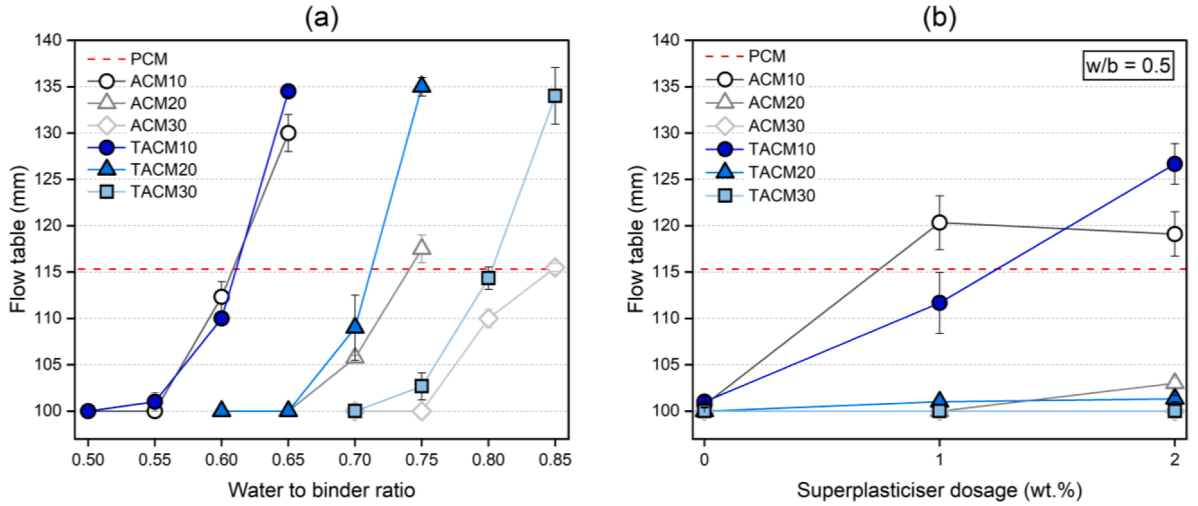

Fig. 8. Effect of APS on (a) water demand; and (b) superplasticizer dosage to achieve comparable flow to reference mortar at 0.5 w/b ratio. PCM = plain PC mortar; ACM = mortars with as-produced APS; TACM = mortars with thermally treated (900°C) APS.

workability. Overall, mortars with 10 wt.% APS demonstrated the most favourable balance between water demand and flow performance, particularly when combined with SP. At higher replacement levels, both the increased water requirement and limited SP efficiency resulted in reduced flowability.

3.6. *Compressive strength, water absorption and apparent porosity*

The influence of APS on strength development of mortars is presented in Fig. 9. At early ages (first 3 days), ACM10 and TACM10 achieved comparable strengths to the PCM reference. By 7 days, both mixes outperformed PCM, with strengths greater than 50 MPa. However, mortars with 20 wt.% and 30 wt.% APS exhibited slower strength development. This highlights the adverse impact of high APS replacement levels on early strength. By 28 days, mixes with 10 wt.% and 20 wt.% APS achieved strengths that are either comparable or superior to the PCM reference. For example, the 28-day strength of ACM10 was 30% higher than PCM. At later ages, ACM10 experienced a further modest strength increase to 67.2 MPa at 90 days. Mortars with 30 wt.% APS showed significantly lower compressive strengths compared to other mixes across all ages. It is worth noting that strength development in APS-containing mortars does not solely reflect pozzolanic reactivity. In high-APS mixes, the reduced flowability is likely to influence compaction and therefore the pore structure and final strength. Although

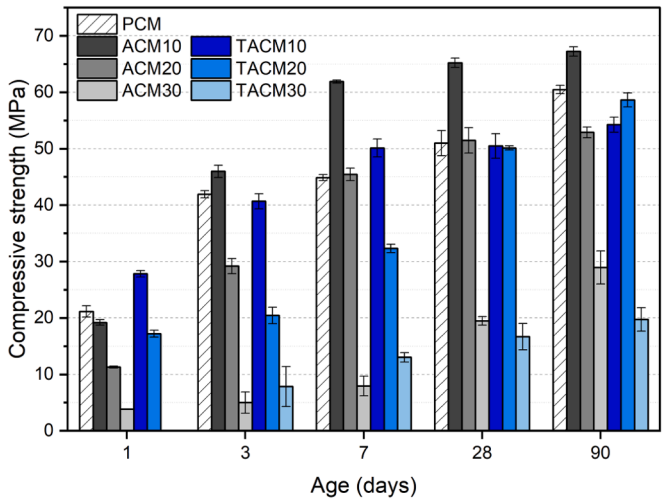

Fig. 9. Compressive strength development of mortars up to 90 days curing at 0.5 w/b ratio. PCM = plain PC mortar; ACM = mortars with as-produced APS; TACM = mortars with thermally treated (900°C) APS.

thermal treatment reduced water demand, this was not sufficient to fully compensate the adverse effects of workability loss at high APS replacement levels.

Water absorption and porosity measurements were conducted at 7 days to provide insight into early microstructural development and its relationship with compressive strength. This age was selected because AC10 and AC20 showed the most distinct strength response relative to the control mix. The results show that PCM and ACM10 had similar water absorption and apparent porosity at ~8 wt.% and ~17.5 vol.% respectively. However, other mortars recorded higher water absorption and porosity, which increased with APS content. For example, the porosity of ACM30 was more than double than that of PCM and ACM10, and ~1.7 times higher than ACM20. The strength performance of mortars with thermally treated APS is consistent with their observed workability (Section 3.5), suggesting similar effects. These observations show that mixes with high APS content (above 20 wt.%) experienced incomplete compaction due to its much-reduced workability, which contributed to higher porosity and absorption and, in turn, lower strength. This identifies 20 wt.% as the practical upper limit for APS in its current form and highlights where mix design improvements are needed.

4. Discussion

The combined results from TGA, Q-XRD, FTIR, and BET highlight four thermally induced stages in APS evolution. Below 500°C, only physically adsorbed water is lost, with no significant structural change, as confirmed by stable SSA, pore volume, and FTIR spectra. Between 500–750°C, progressive dehydroxylation begins [49,50], indicated by reduced Si–OH and OH-related FTIR signals, along with pore enlargement and SSA reduction. These changes align with the formation of amorphous clinochlore and initial silica network restructuring [51–53]. In the 750–900°C range, chabazite and cordierite convert to amorphous phases, with further silanol condensation and minimal disruption to the silica backbone. The increase in average pore diameter with constant SSA suggests pore coalescence or collapse. At 1000°C, extensive dehydroxylation and pore closure result in a sharp decline in SSA and reduced pore volume, indicating significant network densification [48,49,50–52]. These observations confirm that thermal treatment enhances the reactivity of APS by reducing hydroxylation and partially restructuring the pore network. However, it does not eliminate the high SSA, which continues to pose challenges in terms of water demand and workability, particularly at high replacement levels. From a practical standpoint, these findings suggest that extensive thermal treatment on APS would not be beneficial. The added processing steps would increase complexity and energy use without offering substantially improved performance over the as-produced material.

APS demonstrates pozzolanic reactivity that increases with thermal treatment, but remains lower than that of microsilica. This is because APS contains residual crystalline phases, while microsilica is completely amorphous. While the R^3 test classifies APS as moderately reactive, the strength performance, particularly at 10–20 wt.% replacement, exceeds expectations based on calorimetric thresholds. This divergence reflects the limitation of using single-point calorimetry metrics (e.g., 330 J/g at 7 days) to predict SCM performance. The strength enhancement, especially at low replacement level, is attributed not only to pozzolanic activity but also to filler effects, nucleation, and pore refinement. Such mechanisms are not captured by calorimetry, and similar critiques have been made for other SCMs, including calcined clays in LC3 systems. It is also noted that despite the higher R^3 value of the 900°C material, as-produced APS gave higher strengths, indicating that increased reactivity in the R^3 test does not necessarily translate into improved mechanical performance. These insights reinforce the need for a multi-parameter evaluation framework that considers chemical, physical, and microstructural contributions.

The high SSA of APS enhances initial dissolution but simultaneously increases water demand and reduces ionic mobility, which can limit reactivity. The persistence of silanol groups may also contribute to early Ca^{2+} binding and premature surface passivation. At high replacement levels, these effects combine to reduce hydration, as reflected in the retention of unreacted C_3S and elevated porosity. In contrast, at moderate (10–20 wt.%) levels, APS provides both reactivity and beneficial physical effects, improving strength and potentially other properties. The high SSA and water demand of APS remains a major constraint and is directly linked to the limit of 20% replacement identified in this study. The fine irregular particles increase paste viscosity, which narrows the workable range of the mix. This, together with the steps required to produce APS from olivine, represents a practical challenge when compared to established SCMs such as calcined clay, and that needs to be addressed in future work.

APS derived from olivine is viable as a next-generation low-carbon SCM, particularly when the production process and potential environmental benefits are considered. APS production from olivine uses a globally abundant raw material and a simple chemical treatment process. Other SCMs like fly ash or silica fume, rely on waste streams from energy-intensive industries. Compared to hydrochloric acid leaching or multi-step processes [12], the single-step sulphuric acid leaching process used simplifies APS production from olivine while achieving comparable performance to conventional SCMs at 20 wt.% replacement levels.

A potential limitation is that olivine has variable composition and this could present a challenge to produce a consistent APS. Olivine can contain fayalite, a high-iron phase, which can influence the reactivity and hydration kinetics of APS. This variability may complicate standardisation efforts and affect hydration behaviour in cementitious systems. Addressing this variability requires further research using olivine from diverse sources to evaluate the scalability of APS production. Future research should also investigate a broader range of mix designs to identify optimal parameters for APS utilisation in cementitious systems.

Another limitation of this study is the focus on binary systems (APS and PC). Ternary systems, such as incorporating APS with limestone fillers, could mitigate some of the challenges posed by high SSA and water demand. Limestone fillers have lower SSA and this could help offset the high-water demand and workability loss associated with APS. As a filler, limestone could also reduce PC content while maintaining mechanical performance. Further investigations into ternary systems will be carried to improve the fresh and hardened properties of APS-containing cementitious materials.

Despite these challenges, APS shows promise as a low-carbon SCM. The proposed production route in this study involves energy use and

reagent inputs, and these need to be considered when assessing its overall carbon impact. The acid leaching of olivine generates magnesium sulphate as a by-product, which can be used to sequester CO_2 via carbonation and could help offset the carbon footprint associated with APS production [20]. We are currently examining routes for sulfuric acid recovery and conducting a full life cycle assessment work to establish the net carbon balance. This will help establish and guide the development of APS from olivine as a material that could support more sustainable cementitious systems.

5. Conclusion

Amorphous precipitated silica (APS) derived from olivine exhibits pozzolanic reactivity, reacting with portlandite to form hydration products such as C-S-H and AFt, as confirmed through TGA-MS, Q-XRD, FTIR and R^3 testing. Mortars at 0.5 w/b ratio containing APS at cement replacement levels of 10 wt.% achieved 30% higher compressive strength compared to the control Portland cement mortar at 28 days (50 MPa). Mortars with 20 wt.% APS achieved comparable 28-day compressive strength to the control mortar. Higher replacement levels were limited by elevated water demand, reduced workability and insufficient portlandite to sustain pozzolanic reaction.

The APS was thermally treated between 400 and 1000°C to modify its pore structure, specific surface area (SSA), phase composition and reactivity. Thermal treatment at 750°C and above reduced the SSA and water demand, increased amorphous content and enhanced pozzolanic activity, from moderate to high reactivity with R^3 cumulative heat > 330 J/g at 7 days. Q-XRD and FTIR results confirmed dehydroxylation and structural densification as the primary mechanisms underlying these changes. While SSA and water demand reductions were observed, improvements in workability were modest and this influenced strengths at high replacement levels (30 wt.%). As produced APS provides a simpler and more energy-efficient option to incorporate into cementitious systems at moderate replacement levels up to 20 wt.%.

While APS derived from olivine has potential as an SCM, significant challenges remain. These include high water demand, the variability in raw material composition and limitations associated with binary cementitious systems. Future research will focus on exploring ternary systems, including blends incorporating limestone, optimising the water-to-binder ratio and mix design to further enhance performance.

CRediT authorship contribution statement

Pei B. Ong: Writing – original draft, Methodology, Investigation, Formal analysis. **Yixiu Zhuge:** Writing – review & editing, Investigation, Formal analysis. **Christopher Cheeseman:** Writing – review & editing, Visualization, Supervision. **Hong S. Wong:** Writing – review & editing, Visualization, Supervision, Funding acquisition, Conceptualization.

Declaration of competing interest

The authors declare that they have no known competing financial interests or personal relationships that could have appeared to influence the work reported in this paper.

Acknowledgements

This work was funded by the Department for Energy Security and Net Zero (DESNZ), under project number CCUS 2106 of the CCUS Innovation 2.0 call – part of the Net Zero Innovation Portfolio (NZIP). The research leading to this publication benefitted from EPSRC funding under grant No. EP/R010161/1 and from support from the UKCRIC Coordination Node, EPSRC grant number EP/R017727/1, which funds UKCRIC's ongoing coordination. The authors would like to thank Marcus Yio, Noel Djobo and Jianhang Feng for their technical support and general discussions.

Data availability

Data will be made available on request.

References

[1] IEA, Cement Tracking Report, 2021. https://iea.blob.core.windows.net/cbaa3da1-fd61-4c2a-8719-31538f59b54f/TechnologyRoadmapLowCarbonTransitionintheCementIndustry.pdf.
[2] IEA, Technology Roadmap: Low-Carbon Transition in the Cement Industry, 2018. https://www.iea.org/reports/technology-roadmap-low-carbon-transition-in-the-cement-industry.
[3] GCCA, The GCCA 2050 Cement and Concrete Industry Roadmap for Net Zero Concrete, 2021. https://gccassociation.org/concretefuture/.
[4] S. Pamenter, R.J. Myers, Decarbonizing the cementitious materials cycle: a whole-systems review of measures to decarbonize the cement supply chain in the UK and European contexts, J. Ind. Ecol. 25 (2021) 359–376, https://doi.org/10.1111/jiec.13105.
[5] IPCC, Guidance Note on Uncertainty, 2021. https://www.ipcc.ch/site/assets/uploads/2018/05/uncertainty-guidance-note.pdf.
[6] G.V.P. Bhagath Singh, V. Durga Prasad, Environmental impact of concrete containing high volume fly ash and ground granulated blast furnace slag, J. Clean. Prod. 448 (2024) 141729, https://doi.org/10.1016/j.jclepro.2024.141729.
[7] B. Pacewska, I. Wilińska, Usage of supplementary cementitious materials: advantages and limitations. Part I: C–S–H, C–A–S–H and other products formed in different binding mixtures, J. Therm. Anal. Calorim. 142 (2020) 371–393, https://doi.org/10.1007/s10973-020-09907-1.
[8] X. Liu, W. Yan, Current advances in slag foaming processes toward reduced CO_2 emission for electric arc furnace steelmaking, J. CO2 Util. 90 (2024) 102979, https://doi.org/10.1016/j.jcou.2024.102979.
[9] L. Muhmood, S. Vitta, D. Venkateswaran, Cementitious and pozzolanic behavior of electric arc furnace steel slags, Cem. Concr. Res. 39 (2009) 102–109, https://doi.org/10.1016/j.cemconres.2008.11.002.
[10] S. Barbhuiya, F. Kanavaris, B.B. Das, M. Idrees, Decarbonising cement and concrete production: strategies, challenges and pathways for sustainable development, J. Build. Eng. 86 (2024) 108861, https://doi.org/10.1016/j.jobe.2024.108861.
[11] A. Scott, C. Oze, V. Shah, N. Yang, B. Shanks, C. Cheeseman, A. Marshall, M. Watson, Transformation of abundant magnesium silicate minerals for enhanced CO_2 sequestration, Commun. Earth Environ. (2021), https://doi.org/10.1038/s43247-021-00099-6.
[12] V. Shah, A. Scott, Pozzolanic characteristics of silica recovered from olivine, Constr. Build. Mater. 332 (2022) 127378, https://doi.org/10.1016/j.conbuildmat.2022.127378.
[13] Y.X. Chen, Y. Hendrix, K. Schollbach, H.J.H. Brouwers, A silica aerogel synthesized from olivine and its application as a photocatalytic support, Constr. Build. Mater. 248 (2020) 118709, https://doi.org/10.1016/j.conbuildmat.2020.118709.
[14] D.J. Lieftink, J.W. Geus, The preparation of silica from the olivine process and its possible use as a catalyst support, J. Geochem. Explor. 62 (1998) 347–350, https://doi.org/10.1016/S0375-6742(97)00067-8.
[15] A. Lazaro, H.J.H. Brouwers, G. Quercia, J.W. Geus, The properties of amorphous nano-silica synthesized by the dissolution of olivine, Chem. Eng. J. 211–212 (2012) 112–121, https://doi.org/10.1016/j.cej.2012.09.042.
[16] R.C.L. Jonckbloedt, The dissolution of olivine in acid – a cost effective process for the elimination of waste acids, 1997.
[17] A. Lazaro, Y.X. Chen, C. Verhoeven, Y. Hendrix, One-step synthesis of ordered mesoporous silica from olivine and its pore size tailoring, J. Clean. Prod. 238 (2019) 117951, https://doi.org/10.1016/j.jclepro.2019.117951.
[18] Y.X. Chen, S. Li, B. Mezari, E.J.M. Hensen, R. Yu, K. Schollbach, H.J.H. Brouwers, Q. Yu, Effect of highly dispersed colloidal olivine nano-silica on early age properties of ultra-high performance concrete, Cem. Concr. Compos. 131 (2022) 104564, https://doi.org/10.1016/j.cemconcomp.2022.104564.
[19] B. Shanks, C. Howe, S. Draper, H. Wong, C. Cheeseman, Carbon capture and storage in low-carbon concrete using products derived from olivine, R. Soc. Open Sci. 11 (2024) 231645, https://doi.org/10.1098/rsos.231645.
[20] B. Shanks, C. Howe, S. Draper, H. Wong, C. Cheeseman, Production of low-carbon amorphous SiO_2 for use as a supplementary cementitious material and nesquehonite from olivine, Mater. Lett. 361 (2024) 136133, https://doi.org/10.1016/j.matlet.2024.136133.
[21] N. Raza, W. Raza, S. Madeddu, H. Agbe, R.V. Kumar, K.H. Kim, Synthesis and characterization of amorphous precipitated silica from alkaline dissolution of olivine, RSC Adv. 8 (2018) 32651–32658, https://doi.org/10.1039/C8RA06257A.
[22] T. Murakata, S. Sato, T. Ohgawara, T. Watanabe, T. Suzuki, Control of pore size distribution of silica gel through sol-gel process using inorganic salts and surfactants as additives, J. Mater. Sci. 27 (1992) 1567–1574, https://doi.org/10.1007/BF00542919.
[23] M. Naddaf, R. Al-Shatter, H. Harmlani, T. Jeejan, Structural and morphological properties of silica extracted from wild oat straw: Effect of post-thermal treatment, Inorg. Mater. 59 (2023) 1034–1043, https://doi.org/10.1134/S0020168523090091.
[24] S. Li, S. Yang, S. Xu, Q. Wan, Influence of heat treatment on the microstructure and surface groups of Stöber silica, Mater. Res. Express 10 (2023) 105004, https://doi.org/10.1088/2053-1591/acff3e.

[25] Z. El Rassi, C. Gonnet, Surface modification of silica gels. Evaluation of thermally treated commercial silica gels, J. Liq. Chromatogr. 3 (1980) 179–199, https://doi.org/10.1080/01483918008060164.
[26] T. Ding, S. Zhang, M. Yio, H. Wong, C. Cheeseman, Engineering aluminosilicates with high surface area extracted from waste concrete to form a viable supplementary cementitious material, Constr. Build. Mater. 462 (2025) 139981, https://doi.org/10.1016/j.conbuildmat.2025.139981.
[27] J. Li, M. Du, Y. Cheng, S. Wang, J. Chen, S. Hu, H. Zhang, H. Zhang, Condensation and hydrophobicity of the surface hydroxyl groups between organosilane-modified water glass and microsilica, Ceram. Int. 49 (2023) 21278–21286, https://doi.org/10.1016/j.ceramint.2023.03.256.
[28] J. Engelbrecht, M. Günther, H. von Wallis, Use of silica gel with a reduced surface as a filler for dental mass material, Patent, 1983.
[29] R. Snellings, J. Chwast, Ö. Cizer, N. De Belie, Y. Dhandapani, P. Durdzinski, J. Elsen, J. Haufe, D. Hooton, C. Patapy, M. Santhanam, K. Scrivener, D. Snoeck, L. Steger, S. Tongbo, A. Vollpracht, F. Winnefeld, B. Lothenbach, RILEM TC-238 SCM recommendation on hydration stoppage by solvent exchange for the study of hydrate assemblages, Mater. Struct. 51 (2018) 172, https://doi.org/10.1617/s11527-018-1298-5.
[30] ASTM C1897-20, Standard Test Methods for Measuring the Reactivity of Supplementary Cementitious Materials by Isothermal Calorimetry and Bound Water Measurements, ASTM International, West Conshohocken, PA, 2020.
[31] BS EN 12350-5:2019, Testing Fresh Concrete – Part 5: Flow Table Test, BSI, London, 2019.
[32] ASTM C642-21, Standard Test Method for Density, Absorption, and Voids in Hardened Concrete, ASTM International, West Conshohocken, PA, 2022.
[33] J.N.Y. Djobo, D. Stephan, The reaction of calcium during the formation of metakaolin phosphate geopolymer binder, Cem. Concr. Res. 158 (2022) 106840, https://doi.org/10.1016/j.cemconres.2022.106840.
[34] E.A. Paukshtis, M.A. Yaranova, I.S. Batueva, B.S. Bal'zhinimaev, An FTIR study of silanol nests over mesoporous silicate materials, Microporous Mesoporous Mater. 288 (2019) 109582, https://doi.org/10.1016/j.micromeso.2019.109582.
[35] S.Y. Purwaningsih, A. Riyanto, S. Machmudah, H.E. Sentosa, S. Pratapa, Simultaneous synthesis of silica polymorphs and activated carbon from rice husk, Silicon 16 (2024) 3063–3072, https://doi.org/10.1007/s12633-024-02881-5.
[36] Y. Liang, H. Zhang, H. Ding, S. Sun, Y. Wang, X. Bai, S. Li, Amorphous silica: Prepared by by-product microsilica in ferrosilicon production and applied in amorphous silica–TiO_2 composite with favourable pigment properties, J. Mater. Res. Technol. 26 (2023) 235–245, https://doi.org/10.1016/j.jmrt.2023.07.179.
[37] R. Ellerbrock, M. Stein, J. Schaller, Comparing amorphous silica, short-range-ordered silicates and silicic acid species by FTIR, Sci. Rep. 12 (2022) 11708, https://doi.org/10.1038/s41598-022-15882-4.
[38] S. Zhang, S. Tie, F. Zhang, Cristobalite formation from the thermal treatment of amorphous silica fume recovered from the metallurgical silicon industry, Micro Nano Lett. 13 (2018) 1465–1468, https://doi.org/10.1049/mnl.2018.5167.
[39] S. Kamari, F. Ghorbani, Extraction of highly pure silica from rice husk as an agricultural by-product and its application in the production of magnetic mesoporous silica MCM-41, BioMass Convers. Biorefin. 11 (2021) 3001–3009, https://doi.org/10.1007/s13399-020-00637-w.
[40] A.V. Syugaev, K.A. Yazovskikh, S.F. Lomayeva, A.A. Shakov, A.N. Maratkanova, Formation, characterization and protective properties of organic/silicate hybrid shells on flaky Fe–Si–Al particles obtained by wet ball milling, Colloids. Surf. A Physicochem. Eng. Asp. 622 (2021) 126692, https://doi.org/10.1016/j.colsurfa.2021.126692.
[41] R. Salsabila, M. Khair, E.Saputra Ardi, Green synthesis of silica gel adsorbents: microwave boosts silanol groups for improved moisture uptake, Braz. J. Dev. 10 (2024) 644–652, https://doi.org/10.34117/bjdv10n1-039.
[42] O.K. Cakmak, K.T. Hassan, J. Wang, X. Han, L. Šiller, Synthesis of sodium silicate-based silica aerogels with graphene oxide by ambient pressure drying, J. Porous Mater. 28 (2021) 1545–1552, https://doi.org/10.1007/s10934-021-01103-2.
[43] T. Lv, J. Zhang, L. Xu, D. Hou, W.J. Long, B. Dong, Hydration behavior and chloride binding of seawater-mixed sintered sludge cement paste: experimental and thermodynamic study, Constr. Build. Mater. 426 (2024) 136170, https://doi.org/10.1016/j.conbuildmat.2024.136170.
[44] A. Carrillo García, M. Latifi, J. Chaouki, Kinetic study of calcination of a rare earth ore, Hydrometallurgy 200 (2021) 105557, https://doi.org/10.1016/j.hydromet.2021.105557.
[45] J.L. Stakebake, Characterization of natural chabazite and 5A synthetic zeolites: Part I. Thermal and outgassing properties, J. Colloid Interface Sci. 99 (1984) 41–49, https://doi.org/10.1016/0021-9797(84)90083-3.
[46] G. Cruciani, Zeolites upon heating: factors governing their thermal stability and structural changes, J. Phys. Chem. Solids 67 (2006) 1973–1994, https://doi.org/10.1016/j.jpcs.2006.05.057.
[47] D. Londono-Zuluaga, A. Gholizadeh-Vayghan, F. Winnefeld, F. Avet, M. Ben Haha, S.A. Bernal, Ö. Cizer, M. Cyr, S. Dolenec, P. Durdzinski, J. Haufe, D. Hooton, S. Kamali-Bernard, X. Li, A.T.M. Marsh, M. Marroccoli, M. Mrak, Y. Muy, C. Patapy, M. Pedersen, S. Sabio, S. Schulze, R. Snellings, A. Telesca, A. Vollpracht, G. Ye, S. Zhang, K.L. Scrivener, Report of RILEM TC 267-TRM phase 3: validation of the R3 reactivity test across a wide range of materials, Mater. Struct. 55 (2022) 20, https://doi.org/10.1617/s11527-022-01947-3.
[48] H.N. Kim, S.K. Lee, Atomic structure and dehydration mechanism of amorphous silica: insights from 29Si and 1H solid-state MAS NMR study of SiO_2 nanoparticles, Geochim. Cosmochim. Acta 120 (2013) 39–64, https://doi.org/10.1016/j.gca.2013.05.047.
[49] Z. Cheng, H. Shan, Y. Sun, L. Zhang, H. Jiang, C. Li, Evolution mechanism of surface hydroxyl groups of silica during heat treatment, Appl. Surf. Sci. 513 (2020) 145766, https://doi.org/10.1016/j.apsusc.2020.145766.
[50] S. Mohammed, Processing, effect and reactivity assessment of artificial pozzolans obtained from clays and clay wastes: a review, Constr. Build. Mater. 140 (2017) 10–19, https://doi.org/10.1016/j.conbuildmat.2017.02.078.
[51] R. Lemma, C.C. Castellano, V.L. Bonavetti, M.A. Trezza, V.F. Rahhal, E.F. Irassar, Thermal transformation of illitic-chlorite clay and its pozzolanic activity. RILEM Bookseries, Springer, 2018, pp. 266–272, https://doi.org/10.1007/978-94-024-1207-9_43.
[52] A. Khalfaoui, M. Hajjaji, A chloritic–illitic clay from Morocco: temperature–time–transformation and neoformation, Appl. Clay Sci. 45 (2009) 83–89, https://doi.org/10.1016/j.clay.2009.03.006.